

# A New Model for Capillary Condensation–Evaporation Hysteresis Based on a Random Corrugated Pore Structure Concept: Prediction of Intrinsic Pore Size Distribution. 2. Model Application

G. P. Androutsopoulos\* and C. E. Salmas

Department of Chemical Engineering, Section II, Chemical Process Engineering Laboratory, National Technical University of Athens, 9 Heroon Polytechniou Street, GR 15 780 Athens, Greece

A performance assessment of the corrugated pore structure model (CPSM), developed in part 1 (*Ind. Eng. Chem. Res.* 2000, 39, 3747), is carried out through a simulation of experimental gas sorption hysteresis, covering all IUPAC versions and that of the novel MCM-41 materials. The materials studied are an anodic aluminum oxide film, HDS catalysts, montmorillonite, lignite, pillared clays, and MCM-41. CPSM evaluations of pore surface areas are consistent with the pertinent BET estimates while for partly microporous structures approach those obtained by the restricted adsorption BET variant. CPSM predictions of pore size distribution (psd) have been compared with those obtained by the Roberts method. In several examples, the latter method, when applied exclusively to condensation data, yielded psd's approaching the relevant CPSM distributions while, in other examples, by using evaporation data only, deduced psd's comparable to those yielded by the CPSM model. CPSM predictions are in partial agreement with the novel molecular simulation and the NLDFT theories. The CPSM model proved to be a simple, flexible, purely analytical model enabling meaningful predictions of intrinsic psd's and evaluations of a statistical pore shape parameter ( $N_S$ ) related to pore structure tortuosity.

## Introduction

As has been discussed in part 1 of this work (*Ind. Eng. Chem. Res.* 2000, 39, 3747), the conventional methods for the calculation of pore volume and surface area distributions (psd) from gas sorption hysteresis data<sup>1–4</sup> produce similar predictions. The results reported in Table 1 are indicative of the latter observation. Moreover, the methods of psd prediction under consideration yield total pore surface predictions differing from the pertinent BET values. Such deviations may be quite big, ranging from –25% to +51% (Table 2). It is thus quite justified to apply the theory of the CPSM model developed in part 1 of this work and assess the potential of its performance for a good variety of real porous materials. Such materials cover the entire spectrum of hysteresis loop shapes according to IUPAC classification and involve pore structures made up of meso- and/or micropore sizes. Additionally, sorption hysteresis of two MCM-41 nanoporous materials<sup>5,6</sup> will be simulated. A summary of the materials to be studied herewith is presented in Table 3. For each category of porous materials the following aspects will be examined and discussed.

*The BET specific surface area will be calculated for each one of the nitrogen sorption hysteresis loops and the relevant plots will be provided.*

*The Roberts method will be applied to evaluate pore volume and surface area distributions of a specified material by employing separately the experimental data of each one of the hysteresis loop branches. Cylindrical pore geometry, a hemispherical liquid meniscus configuration, and a contact angle  $\theta = 0$  will be assumed. Gas*

sorption hysteresis loop data to be used in psd calculations cover the  $P/P_0$  range from ~0.4 to 1 and the formula to be used<sup>7</sup> for the dependence of the adsorbed gas layer thickness,  $t(\text{nm})$ , upon  $P/P_0$  reads

$$t = 0.35 \left( \frac{5}{\ln(P_0/P)} \right)^{1/3} \quad (1)$$

For each hysteresis loop the maximum surface area as predicted by the Roberts method will be compared graphically to the relevant BET value and the differences will be tabulated and discussed.

*Nitrogen sorption data regression by the CPSM model* will be performed and optimum values of its parameters, i.e.,  $N_S$  and  $b$  (bell-shaped distribution parameter) will be determined.  $N_S$  values reflect pore structure complexity characteristics and may be applied in a novel definition of a pore tortuosity factor. The value of  $b$  determines the intrinsic pore volume distribution function and enables the construction of the respective intrinsic pore segment number and surface area distributions (refer to ref 27 of this work, eqs 32–35). These distributions will be compared to those yielded by the Roberts method and where applicable to novel methods, e.g., the NLDFT method, as part of the procedure to evaluate the CPSM performance. With regard to the variation of the adsorbed gas layer thickness  $t(\text{nm})$  with  $P/P_0$  change, the following formula will be tested:

$$t = n \left( \frac{5}{\ln(P_0/P)} \right)^{1/3} (P/P_0)^m \quad (2)$$

Parameter  $n$  is expected to vary between 0.35 and 0.45<sup>8</sup> while  $m$  is in the range 0–0.28.

*The maximum values of the cumulative pore surface area obtained by the CPSM method will be compared*

\* To whom correspondence should be addressed. Tel.: (+301) 7723225. Fax: (+301) 7723155. E-mail: androuts@orfeas.chemeng.ntua.gr.

**Table 1. Comparison of Specific Surface Areas of HDS Catalysts Deduced from Nitrogen Capillary Condensation-evaporation Data by Applying Four Different Calculation Techniques: BJH, C-I, ML, Rb**

HDS catalyst designation	surface area (m <sup>2</sup> /g) calculated from adsorption, capillary condensation data					surface area (m <sup>2</sup> /g) calculated from desorption, capillary evaporation data				
	BJH	C-I	ML	Rb	mean	BJH	C-I	ML	Rb	mean
Comox 451	215	217	218	217	<b>217</b>	357	361	355	361	<b>359</b>
Harshaw HT-400E	236	238	234	238	<b>237</b>	316	319	314	319	<b>317</b>
ICI-41-6	265	268	263	268	<b>266</b>	374	377	371	377	<b>375</b>
ICI-61-1	223	226	222	225	<b>224</b>	335	338	332	338	<b>336</b>
G-51 (1.5 mm)	231	233	229	233	<b>232</b>	331	333	328	333	<b>331</b>
G-51 (3.0 mm)	297	300	295	299	<b>298</b>	395	399	393	399	<b>397</b>

**Table 2. Comparative Values of Specific Surface Areas for Six HDS Catalysts Predicted by the Roberts Method (Use Is Made of Either Capillary Condensation,  $S_{Rb(co)}$ , or Evaporation Data,  $S_{Rb(ev)}$ )**

HDS catalyst designation	$S_{BET}$	$C$ (BET parameter)	$S_{Rb(co)}$	$S_{Rb(ev)}$	$(S_{Rb(co)} - S_{BET})/S_{BET}$ (%)	$(S_{Rb(ev)} - S_{BET})/S_{BET}$ (%)
Comox 451	289	152	217	361	-25	+25
Harshaw HT-400E	245	242	238	319	-3	+30
ICI-41-6	246	121	248	346	+1	+41
ICI-61-1	224	45	225	338	+0.5	+51
G-51 (1.5 mm)	295	170	233	333	-21	+13
G-51 (3.0 mm)	285	176	299	399	+5	+40

**Table 3. Summary of Porous Materials Studied in This Work (Using the CPSM Model To Simulate Nitrogen Sorption Hysteresis Data)**

hysteresis loop type	description of material
H <sub>1</sub> -type (IUPAC)	<b>Anodic oxide film</b> Preparation (Salmas Doctoral Thesis, under preparation <sup>13</sup> ). Porosimetry measurements, this work. <sup>a</sup>
H <sub>2</sub> -type (IUPAC)	<b>HDS catalysts</b> Commercial grades, Table 7. Porosimetry measurements, this work. <sup>a</sup>
H <sub>3</sub> -type (IUPAC)	<b>Dry lignite</b> Sample preparation and porosimetry measurements, this work. <sup>a</sup>
H <sub>4</sub> -type (IUPAC)	<b>Montmorillonite</b> Literature data. <sup>8</sup>
	<b>Pillared clays</b> Literature data <sup>18,19</sup>
novel nanoporous materials (mesoporous molecular sieves)	<b>MCM-41</b> Literature data <sup>5,6</sup>

<sup>a</sup> A Sorptomatic, Carlo Erba, Model 1800, has been used to carry out the porosimetry measurements.

to BET values as an additional test in evaluating the predictive potential of the method under consideration.

Finally, the improvement of the predictions achieved by the CPSM model will be assessed, in retrospect, with those of the conventional methods.

**Curve-Fitting Method.** On the basis of the CPSM model formulas reported in part 1 of this work, a computer code was written in FORTRAN and run in a PC. For given values of  $N_s$ , BSD parameter  $b$ , and  $D$  vs  $P/P_0$ , theoretical sorption loops can be generated. The variation of CPSM parameters during the development of the IUPAC loop simulations provided good help in the identification of the range of the variation of key CPSM parameters. These data proved quite useful for the fitting of the experimental loops either by trial and error or by a least-squares technique.

**Porous Anodic Aluminum Oxide Film.** *Pore Structure Characteristics of Anodic Aluminum Oxide Films.* Porous anodic aluminum oxide films have been used as test materials for the preparation of inorganic membranes (gas separations, ultrafiltration, etc.<sup>9,10</sup>), catalysts,<sup>11,12</sup> etc. The pore structure of anodic alumina oxide

**Table 4. Data of Porous Anodic Aluminum Oxide Film**

aluminum foil thickness	0.12 mm
aluminum external surface area	28 cm <sup>2</sup> /g
anode dimensions (dipped in electrolyte)	80 × 50 mm
electrolyte	H <sub>2</sub> SO <sub>4</sub> 15% w/w
current intensity through the anode	0.36 A
voltage applied	9.60 V
duration of anodization	84 min
current density	0.45 A/dm <sup>2</sup>
electric charge through the specimen	2268 Cb/dm <sup>2</sup>

films is practically composed of straight, almost constant cross-sectional and nonintersecting pores, of comparable dimensions. The method of preparation is quite simple. When the appropriate anodizing conditions are selected, the desired pore sizes and density (number of pores per unit external surface area) can be achieved. Pore sizes are usually found between 10 and 100 nm while surface pore densities fall in the range 50–1000 pores/ $\mu$ m<sup>2</sup>.

**Anodic Aluminum Oxide Film Preparation.** Anodic oxide film properties and conditions of preparation<sup>13</sup> are summarized in Table 4. Prior to anodic oxidation, the aluminum specimen was washed with ethyl alcohol and its upper part was covered with Teflon film. Following the oxidation, which lasted for 84 min, the specimen was washed with water, an alkaline solution, and water and then dried. Care was taken for a continuous stabilization of the current intensity during anodization. The current density has been kept below 1 A/dm<sup>2</sup> and the electric charge through the specimen below 8500 Cb/dm<sup>2</sup> to avoid formation of nonporous Al<sub>2</sub>O<sub>3</sub>.

**Nitrogen Adsorption, Capillary Condensation, Desorption, and Evaporation Measurements.** Experimental nitrogen sorption hysteresis loop data have been plotted in Figure 1(1-a). Generally, such loops are not expected because these materials possess pores of uniform shape. However, the latter loop is one of several obtained by carrying out a few runs on samples of the same material. It seems that the pore structure of anodic oxides is not as simple and uniform as one could expect and depends on the conditions of anodization (e.g., Figure 6 of ref 14). It should also be noted that sorption hysteresis loops for anodized alumina have been reported (e.g., Figure 2 of ref 15). It is obvious from Figure 1(1-a) that this type of loop is formed by two more or less vertical branches at relatively high  $P/P_0$  values, i.e., higher than 0.7, and falls in the H<sub>1</sub>-type category-

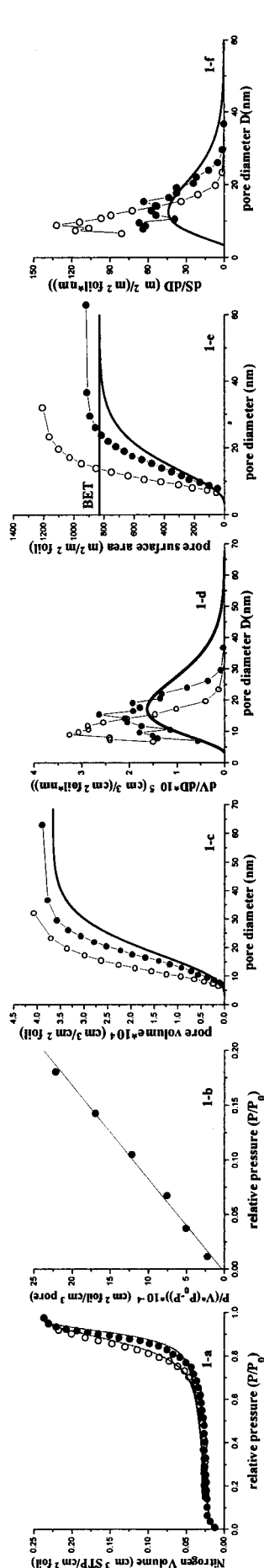


**Figure 1.** (1-a) Nitrogen sorption hysteresis loop for anodic aluminum oxide film (data of sample preparation in Table 4). Continuous line is the CPSM fitting, BET plot (1-b). Pore volume psd (1-c) and (1-d). Surface area psd (1-e) and (1-f). CPSM prediction (solid line), Roberts condensation (●), and Roberts evaporation (○).

according to the IUPAC classification (part 1 of this work). Also in Figure 1 (1-a) the result of CPSM simulation of the experimental points is presented (solid line). This fitting is considered as being a satisfactory theoretical description of the experimentally observed phenomena. CPSM fitting parameters are given in Table 5.

It is apparent from the figures of Table 5 that the fitting of the experimental loop was achieved by taking  $\cos \theta_h = 1$ , i.e., a hemispherical liquid/volume (l/v) interface prevails during the evaporation process. Besides a pseudocylindrical interface ( $\cos \theta_c = 0.68$ , i.e., deviates from the value  $\cos \theta_c = 0.5$  valid for a purely cylindrical geometry) seems to coexist (in terms of eq 25, part 1 of this work) with a hemispherical one during condensation. The enhanced role of the cylindrical interface geometry during condensation in the context of the CPSM model can be attributed to the regular pore shape comprising the pore structure of anodic oxide films and the relatively low value of  $N_S = 4$ . However, pores are independent and blind in one end, a fact favoring the capillary evaporation to proceed through a perfectly hemispherical interface (i.e.,  $\cos \theta_h = 1$ ).

With regard to the multilayer thickness correlation, the best fit of the experimental loop has been achieved for  $n = 0.35$  and  $m = 0.05$  (eq 2), i.e., slightly different from the conventional values (i.e.,  $n = 0.35$  and  $m = 0$  (eq 1)). The BET plot is given in Figure 1(1-b) while cumulative pore volume and surface area distributions, derived by both the CPSM and the Roberts methods, are plotted in Figure 1(1-c),(1-d) together with the pertinent  $S_{BET}$  values. Numerical values for surface areas  $S_{CPSM}$ ,  $S_{Rb(co)}$ ,  $S_{Rb(ev)}$ , and  $S_{BET}$  as well as percentages of surface area deviations from the  $S_{BET}$  value are reported in Table 6. The  $S_{CPSM}$  surface area almost coincides with the  $S_{BET}$  value while  $S_{Rb(co)}$  and  $S_{Rb(ev)}$  showed a clear deviation, i.e., 6.6% and 37.2%, respectively, from the  $S_{BET}$  value.

**Hydrodesulfurization Catalysts.** Porosimetry investigations on samples of six HDS catalysts supplied by four different manufactures have been carried out in the present study. Chemical composition and porosimetry data as provided by the supplier are included in Table 7. An adsorption apparatus (Sorptomatic, Carlo Erba, model 1800) has been used to carry out nitrogen sorption measurements. Values of total pore surface area, determined by four different calculated methods, have been already reported in the Introduction of this work (Table 1).

This section deals with the application of the CPSM model to curve fit the gas sorption hysteresis loop for each one of the catalysts and obtain the values of CPSM parameters. The latter helps the construction of the cumulative pore volume and surface area diagrams. These plots include also the respective pore size distributions calculated by the Roberts method as well as the BET prediction (refer also to BET plots in Figure 2(2-1b)–(2-6b)) of the total specific pore surface area, for comparison reasons. The full set of results is illustrated in Figure 2.

As the plots of Figure 2(2-1a)–(2-6a) indicate, the shape of the experimental hysteresis loops resembles closer the H<sub>2</sub>-type in the IUPAC classification. The CPSM simulation is visualized by the continuous line on the pertinent plots and considered to be quite satisfactory. Numerical values of the CPSM-fitting parameters are provided in Table 8.

**Table 5. CPSM Fitting Parameters (refer to Figure 1 (1-a))**

specimen	$V_{\text{gmax}}^a$ (cm <sup>3</sup> (STP)/cm <sup>2</sup> foil)	$N_s^b$	parameters of the intrinsic pore segment number distribution $F(D)$			Kelvin parameters <sup>c</sup>		adsorbed gas layer thickness parameters, eq 2	
			$b$	$P_c/P_0$	$(P/P_0)_{\text{max}}$	$\cos \theta_c$	$\cos \theta_h$	$m$	$n$
anodic aluminum oxide film	0.237	4.0	-11.65	0.535	0.980	0.68	1.0	0.05	0.35

<sup>a</sup> Measurement carried out in this work (Figure 1(1-a)). <sup>b</sup> Pore cross-sectional variation number. <sup>c</sup> As defined by eq 11 (part 1 of this work).

**Table 6. Surface Area Data for Porous Anodic Aluminum Oxide Film**

specimen	$S_{\text{BET}}$	$C$ (BET parameter)	$S_{\text{Rb(co)}}$	$S_{\text{Rb(ev)}}$	$S_{\text{CPSM}}$	$(S_{\text{Rb(co)}} - S_{\text{BET}})/$ $S_{\text{BET}}$ (%)	$(S_{\text{Rb(ev)}} - S_{\text{BET}})/$ $S_{\text{BET}}$ (%)	$(S_{\text{CPSM}} - S_{\text{BET}})/$ $S_{\text{BET}}$ (%)
anodic aluminum oxide film	830	420	918	1205	830	+10.6	+45.1	0

**Table 7. HDS Catalysts Specifications as Provided by the Noted Supplier**

catalyst identification	supplier	chemical composition			$S_g$ (m <sup>2</sup> /g)	$V_p$ (cm <sup>3</sup> /g)	$d_p$ (mm)
		CoO	MoO <sub>3</sub>	Al <sub>2</sub> O <sub>3</sub>			
Comox 451	Laporte Industries Ltd., England	3.7	12.8	80.41 <sup>a</sup>	300	0.66	1.5
Harshaw HT-400E	Harshaw Chemie Bv, De Meern, The Netherlands	3.0	15.0	82.0	230	0.50	1.5
ICI-41-6	Imperial Chemical Industries, England	3.3	14.0	82.7	250	0.56	1.5
ICI-61-1			nickel oxide-molybdenum oxide-alumina				1.5
G-51 (1.5 mm)	Girdler Sud-Chemie	3.5	10.0	86.5	250 <sup>b</sup>	0.72	1.5
G-51 (3.0 mm)	Katalysator GMBH	3.5	10.0	86.5	250 <sup>b</sup>	0.72	3.0

<sup>a</sup> Balance: SiO<sub>2</sub> = 1.4%, SO<sub>3</sub> = 1.6%, Na<sub>2</sub>O + K<sub>2</sub>O = 0.06%, and Fe = 0.03%. <sup>b</sup> Surface areas determined in this work by the BET method found to be equal to 295 m<sup>2</sup>/g for sample G51-(1.5 mm) and 289 m<sup>2</sup>/g for sample G51-(3.0 mm) (Table 9).

**Table 8. CPSM Fitting Parameters Referring to Hysteresis Loops of Figure 2 (Plots (2-1a)–(2-6a))**

catalyst identification	$V_{\text{gmax}}^a$ (cm <sup>3</sup> (STP)/g)	$N_{\text{S}}^b$	parameters of the intrinsic pore segment number distribution $F(D)$								Kelvin parameters <sup>c</sup>		adsorbed gas layer thickness parameters, eq 2	
			$b_1$	$b_2$	$b_3$	$w_1$	$w_2$	$w_3$	$P_{\text{ce}}/P_0$	$(P/P_0)_{\text{max}}$	$\cos \theta_{\text{c}}$	$\cos \theta_{\text{h}}$	$m$	$n$
Comox 451	304.2	5.8	−70	−15	−1	15	10	10	0.40	0.965	0.65	0.65	0.075	0.39
Harshaw HT-400E	308.1	4.3	−100						0.32	0.990	1.00	1.00	0.100	0.39
ICI-41-6	394.0	4.5	−75	−2		6	1		0.44	0.990	0.80	1.00	0.170	0.44
ICI-61-1	344.0	6.0	−90	−5		12	1		0.44	0.990	0.975	0.975	0.180	0.40
G-51 (1.5 mm)	404.0	3.8	−150	−45	−2.5	15	10	7	0.40	0.9912	0.70	0.70	0.150	0.40
G-51 (3.0 mm)	328.4	4.5	−350	−110		13	10		0.39	0.995	0.90	0.90	0.150	0.43

<sup>a</sup> Measurements carried out in this work (Figure 2, (2-1a)–(2-6a)). <sup>b</sup> Pore cross-sectional variation number. <sup>c</sup> As defined by eq 11 (part 1 of this work).

It is worth noting that for some catalysts the CPSM fitting of the hysteresis loop requires the combination of two or even three unimodal bell-shaped distributions (i.e., intrinsic pore number distribution  $F(b_1, b_2, b_3; D)$ ) to achieve a satisfactory fitting result. It is also useful to realize that the values of  $\cos \theta_c$  and  $\cos \theta_h$  determined for each catalyst indicate the degree of deviation from the ideal values, i.e.,  $\cos \theta_c = 0.5$  and  $\cos \theta_h = 1$ . The values of the CPSM parameter  $N_s$  and those of  $P_c/P_0$  and  $(P/P_0)_{\text{max}}$  are different for each catalyst and reflect the pore structure complexity. Such data may possibly find appropriate use in the prediction of a tortuosity factor in the context of a novel definition.  $N_s$  values vary in the range  $N_s = 4$ –6 while in the majority of the cases  $\cos \theta_c = \cos \theta_h$  with values located closer to  $\cos \theta = 1$  (i.e., pseudohemispherical interface geometry). The latter implies that condensation and evaporation alike proceed through a pseudohemispherical interface and the role of the cylindrical interface has been diminished. These deductions would be attributed, in most of the cases, to the intrinsic psd characteristics (i.e., showing two or three modes) and to the relatively higher values of  $N_s$  compared to those valid for the lignite ( $N_s = 3.5$ ) and montmorillonite ( $N_s = 2.9$ ) (refer to Table 10). The best fit of hysteresis loops of HDS catalysts has been made possible for adsorbed layer thickness  $t$  computed

**Table 9. Comparison of Specific Surface Area (m<sup>2</sup>/g) Data Obtained from Nitrogen Sorption Hysteresis (Figure 2(2-1a)–(2-6a)) for a Series of HDS Catalysts ( $S_{\text{CPSM}}$  versus  $S_{\text{BET}}$ )**

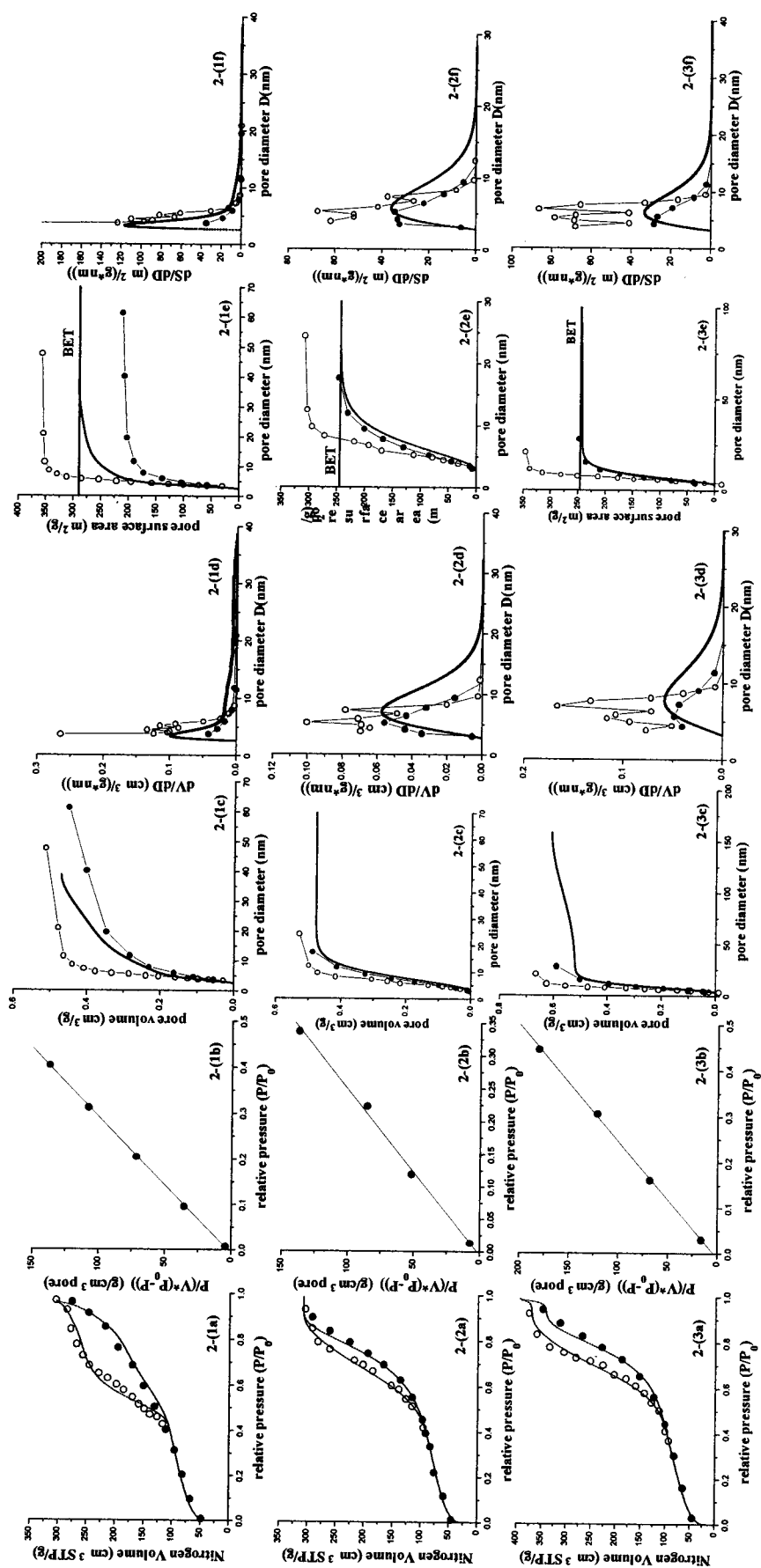
catalyst identification	$S_{\text{BET}}$	$S_{\text{CPSM}}$	$(S_{\text{CPSM}} - S_{\text{BET}})/$ $S_{\text{BET}}$ (%)
Comox 451	289	291	+0.7
Harshaw HT-400E	245	244	-0.4
ICI-41-6	246	246	0
ICI-61-1	224	224	~0.0
G-51 (1.5 mm)	295	295	~0.0
G-51 (3.0 mm)	285	285	~0.0

through eq 3 for  $m = 0.075$ –0.180 and  $n = 0.39$ –0.44. Both parameters deviate appreciably from the usual values ( $m = 0$  and  $n = 0.35$ , eq 1).

The most important result of part 2 (this work) with regard to the HDS catalysts is the comparison of the predictions obtained by the CPSM and the Roberts methods with those of the BET method. A summary of the respective comparisons is presented in Tables 2 and 9.

As a general comment, one can observe that the CPSM predictions are found to be between those by the Roberts method. Indeed, for each one of the catalysts investigated the CPSM predictions of the total pore volume and surface area are higher than those obtained





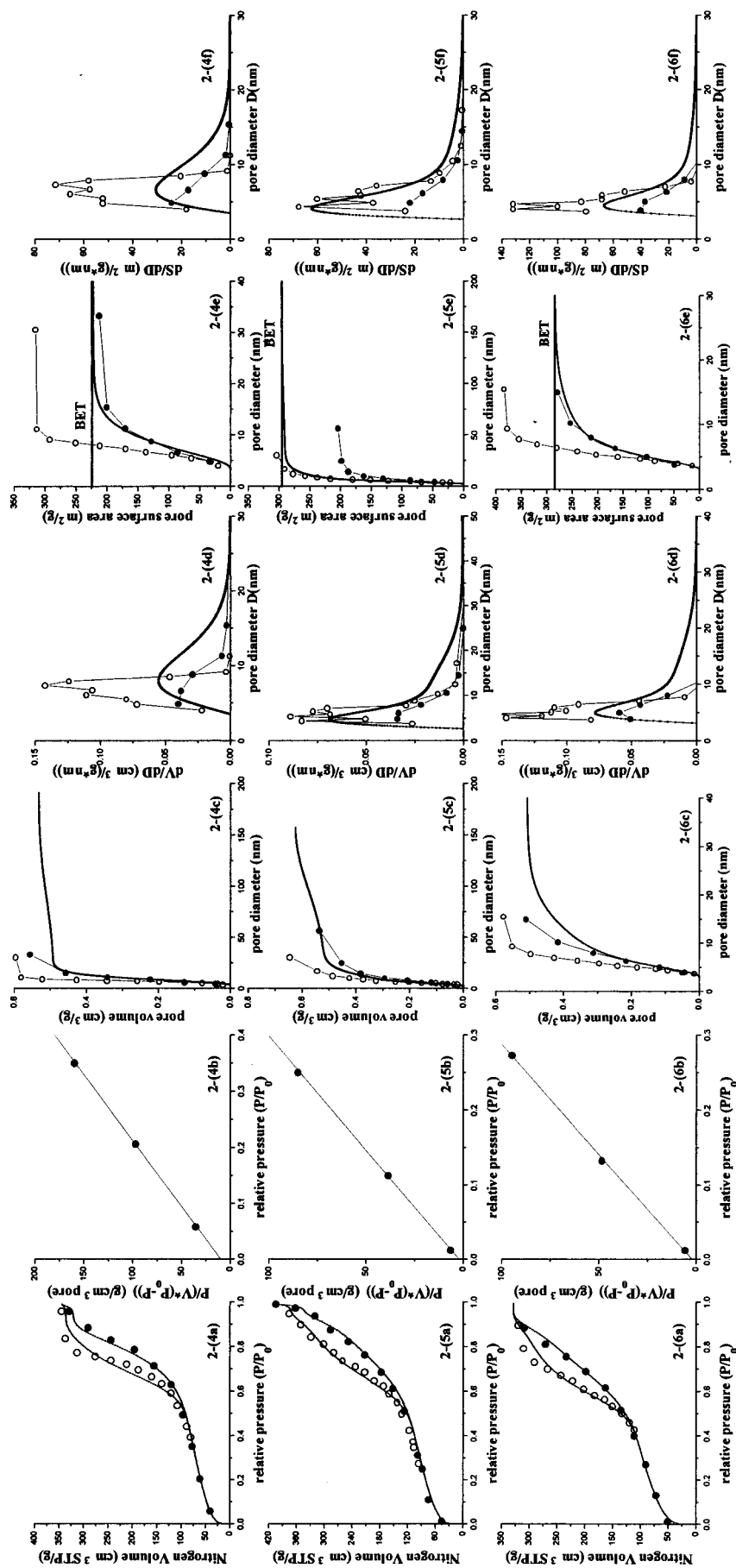


**Figure 2.** Nitrogen sorption hysteresis data for six HDS catalysts. Graphs (2-1a)–(2-6a) provide nitrogen sorption experimental points and the CPSM loop simulation (solid line). BET plots are shown in (2-1b)–(2-6b). Cumulative and differential pore volume psd's are depicted in plots (2-1c)–(2-6c) and (2-1d)–(2-6d), respectively. Cumulative and differential surface area psd's are shown in (2-1e)–(2-6e) and (2-1f)–(2-6f) plots, respectively. CPSM prediction (solid line), Roberts condensation (●), and Roberts evaporation (○).

**Table 10. CPSM Fitting Parameters Referring to Hysteresis Loops of Figure 3(3-1a)–(3-2a)**

specimen	$V_{\text{gmax}}^a$ (cm <sup>3</sup> (STP)/g)	$N_S^b$	parameters of the intrinsic pore segment number distribution $F(D)$						Kelvin parameters <sup>c</sup>		adsorbed gas layer thickness parameters, eq 2	
			$b_1$	$b_2$	$w_1$	$w_2$	$P_{\text{ce}}/P_0$	$(P/P_0)_{\text{max}}$	$\cos \theta_c$	$\cos \theta_h$	$m$	$n$
dry lignite	12.876	3.3	−5400	−559	35	1000	0.25	0.9996	0.65	0.65	0.10	0.35
montmorillonite	48	2.90	−5000	−110	1	26	0.45	0.9980	0.60	0.60	0.10	0.35

<sup>a</sup> Measurement carried out in this work (Figure 3 (3-1a)–(3-2a)). <sup>b</sup> Pore cross-sectional variation number. <sup>c</sup> As defined by eq 11 (part 1 of this work).

**Table 11. Surface Area (m<sup>2</sup>/g) Data for Dry Lignite, Figure 3 (3-1e) and Montmorillonite Figure 3(3-2e)**

specimen	$S_{\text{BET}}$	$C$ (BET parameter)	$S_{\text{Rb(co)}}$	$S_{\text{Rb(ev)}}$	$S_{\text{CPSM}}$	$(S_{\text{Rb(co)}} - S_{\text{BET}})/$ $S_{\text{BET}}$ (%)	$(S_{\text{Rb(ev)}} - S_{\text{BET}})/$ $S_{\text{BET}}$ (%)	$(S_{\text{CPSM}} - S_{\text{BET}})/$ $S_{\text{BET}}$ (%)
dry lignite	5.3	103	3.4	7.4	5.3	−35.8	+39.6	0
montmorillonite	20.4	72	10.0	23.0	20.4	−51.0	+12.7	−1.2

by Roberts condensation and lower than those by Roberts evaporation located closer to either the one or the other. These observations lead to the conclusion that we cannot rely on one or the other branch of the hysteresis loop as the conventional methods of psd determination do. The application of a method that uses the data of the entire loop simultaneously constitutes the basis for a unique prediction. The CPSM model is a possible approach for achieving it. Moreover, total pore surface areas (i.e., final point of the pore surface distribution) predicted by the conventional methods, e.g., Roberts, deviate from the BET prediction. In the majority of the cases Roberts evaporation gave the highest differences from the pertinent BET values. This can be attributed to the pore networking effect that is expected to be significant along the capillary evaporation line.

**Porous Materials Bearing Nitrogen Sorption Hysteresis of H<sub>3</sub>-Type (IUPAC).** *Dry Lignite.* (1) *Lignite Sample Characteristics.* The lignite material used in the present study has been sampled from the Megalopolis area (Greece) and its proximate analysis is as follows: moisture 60%, mineral matter (ash) 16%, volatile matter 17%, and fixed carbon the balance (7%) (w/w, as-received basis). The sample consisted of particle sizes  $d_p = +5$ –10 mm and has been subjected to drying under vacuum, at 200 °C for 1 h. Considerable particle size contraction and a weight loss of 59.3% (equivalent to the total moisture content) have been observed during drying.

(2) *Pore Structure Measurements.* Nitrogen sorption measurements at liquid nitrogen temperature yielded the hysteresis loop of Figure 3(3-1a) (dots) which is obviously an H<sub>3</sub>-type (IUPAC). The BET plot (Figure 3(3-1b)) predicts a specific surface area,  $S_{\text{BET}} = 5.3$  m<sup>2</sup>/g, that is considered quite small for such a material. This result is attributed to the activated diffusion phenomena accompanying sorption measurements carried out at such low-temperature values.<sup>16</sup> It is clear from Figure 3(3-1d) that 90% of the surface area is found in the mesopore size range, i.e., 6–30 nm, with a mean pore diameter of about 16 nm. Comparable mesopore surface areas, i.e.,  $10 \pm 3$  m<sup>2</sup>/g (total surface area 179 m<sup>2</sup>/g) determined by small-angle X-ray scattering (SAXS) on Illinois No. 6 coal have been reported.<sup>17</sup> The interest in the present study is concentrated in the exploitation of this particular loop shape features rather than actual values of the pore sizes.

The application of the CPSM model in curve-fitting trials resulted in a very satisfactory simulation as shown in Figure 3(3-1a). Fitting parameters are supplied in Table 10. The most accurate fitting of the

hysteresis data has been achieved for a small value of  $N_S = 3.5$ , indicating a structure made up of pores with relatively reduced frequency of pore cross-sectional variation. A bimodal  $F(D)$  has been considered while bimodality cannot be traced in the pore volume (Figure 3(3-1c)) and the surface area (Figure 3(3-1d)) distributions. The values of  $\cos \theta_c$  and  $\cos \theta_h$  indicate that both capillary condensation and evaporation proceed through l/v interface geometry approaching the cylindrical geometry extreme (e.g.,  $\cos \theta = 0.5$ ) rather than the value  $\cos \theta = 1$  valid for a hemispherical interface geometry (part 1 of this work, eq 11). The pore structure and texture characteristics of such a naturally occurring material may favor such a behavior that can be attributed to the low value of  $N_S = 3.5$ . Adsorbed layer thickness parameters (eq 2) were found to be  $m = 0.1$  and  $n = 0.35$ , approaching the normal values  $m = 0$  and  $n = 0.35$  (eq 1).

Pore volume and surface area distributions as predicted by the Roberts method (condensation and evaporation data) as well as those evaluated by the CPSM model are portrayed in Figure 3(3-1c),(3-1d). These figures reveal that CPSM predictions are located between the psd's deduced by Roberts method.

Comparisons of  $S_{\text{CPSM}}$ ,  $S_{\text{Rb(co)}}$ , and  $S_{\text{Rb(ev)}}$  with the  $S_{\text{BET}}$  are tabulated in Table 11 which records the considerable deviation (>35%) of the surface area predictions made by Roberts method compared to the relevant BET pore surface area evaluation. CPSM model pore surface area predictions are in good agreement with the BET values.

*Montmorillonite.* Nitrogen sorption hysteresis for a montmorillonite sample (Figure 3(3-2a)) has been reported in Gregg and Sing,<sup>8</sup> p 132, Figure 3.17(a). It is clear that this type of hysteresis belongs to the H<sub>3</sub>-type (IUPAC) group. The BET plot of Figure 3(3-2b) indicates the value  $S_{\text{BET}} = 20.4$  m<sup>2</sup>/g. The CPSM fitting of the loop (Figure 3(3-2a) solid line) has been successful and the fitting parameters are reported in Table 10.

These values in their majority are close to those used in the fitting of the lignite data and similar comments can be made with regard to the pore structure characteristics, i.e., pore cross-sectional variation (small  $N_S = 2.9$ ), bimodal nature of  $F(D)$ , same adsorbed gas layer thickness variation with  $P/P_0$ , and a pseudocylindrical l/v interface geometry (i.e.,  $\cos \theta = 0.6$  for both nitrogen capillary condensation and evaporation). The resemblance of the experimental hysteresis loop for the two materials under consideration is reflected in the convergence of the CPSM parameters estimated for best fit, as noted in Table 10.

Cumulative pore volume and surface area distributions, derived from the sorption data of Figure 3(3-2a)

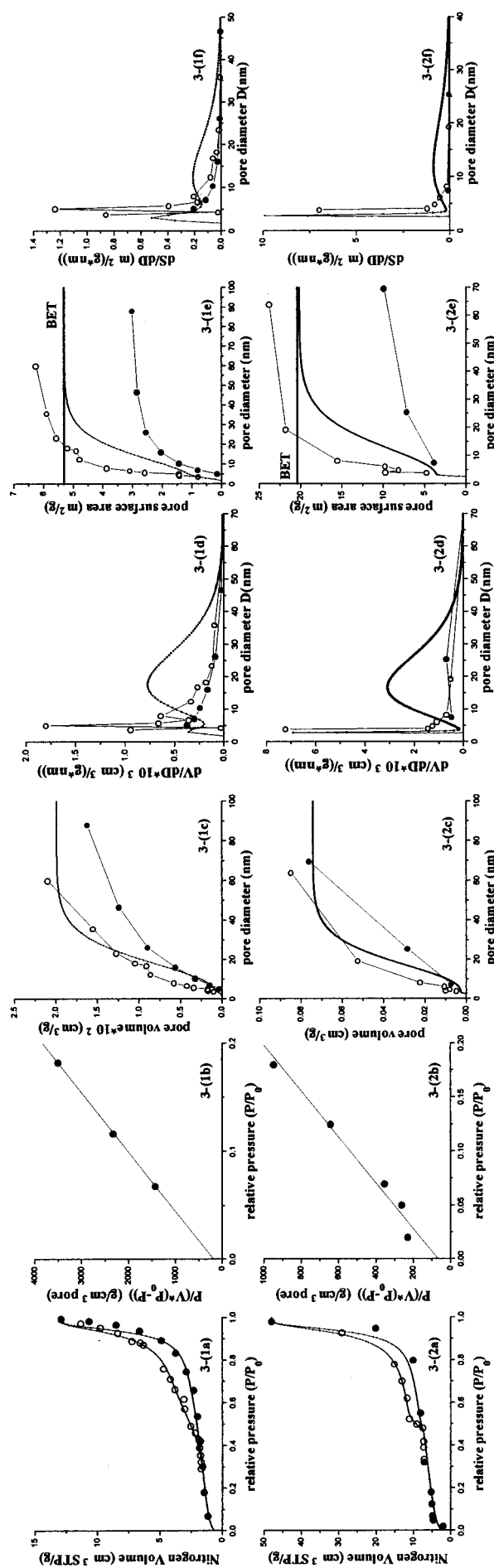


**Figure 3.** Nitrogen sorption hysteresis data (i.e., (3-1a) for lignite, (3-2a) for pillared clay), BET plots (3-1b)–(3-2b), Cumulative and differential pore volume PSD plots (3-1c)–(3-2c) and (3-1d)–(3-2d). Cumulative and differential surface area PSD data in (3-1e)–(3-2e) and (3-1f)–(3-2f) plots. CPSM prediction (solid line), Roberts prediction (dashed line), and Roberts evaporation (○).

by Roberts as well as CPSM methods, are shown in Figure 3(3-2c), (3-2d), respectively. Comparisons of  $S_{\text{CPSM}}$ ,  $S_{\text{Rb(co)}}$ , and  $S_{\text{Rb(ev)}}$  with the  $S_{\text{BET}}$  are tabulated in Table 11.

The  $S_{\text{BET}}$  of montmorillonite, a natural material, is about 4 times higher than that of lignite. Roberts surface area predictions deviate substantially from the corresponding BET value, which is located closer to the  $S_{\text{Rb(ev)}}$  prediction. The  $S_{\text{CPSM}}$  value obtained through the best fit of the experimental points is almost the same with the  $S_{\text{BET}}$  value, deviating by  $-1.2\%$  only.

**Pillared Clays. Nitrogen Sorption.** Two literature hysteresis loops<sup>18,19</sup> (Figure 4(4-1a), (4-2a) dots) concern samples of two different pillared clays bearing a mixed micro-/mesopore structure. It is readily seen from Figure 4 that these two loops can be classified as  $H_4$ -type (IUPAC). The nitrogen sorption data of Figure 4(4-1a) refer to a sample of a pillared clay (A) prepared from Greek montmorillonite bearing pillars of  $\text{AlO}_x$ .<sup>18</sup> The sorption data of Figure 4(4-2a) refer to a pillared clay (B) composed of the basic material and pillars of  $\text{AlO}_x/\text{FeO}_x = 50/50\text{-Z}$ .<sup>19</sup>

**BET Specific Surface Area Evaluation.** As demonstrated in part 1 of this work, the BET equation (eq 34), valid for the monolayer adsorption, yields more meaningful predictions of specific surface area than the conventional BET equation for multilayer adsorption when micropores adsorption data are processed. As noted in Table 13,  $S_{\text{BET(mu)}}$  and  $S_{\text{BET(mo)}}$  deviate by  $S_{\text{BET(mu)}} - S_{\text{BET(mo)}}/S_{\text{BET(mo)}} = -10.2\%$  for pillared clay A and by  $-22.7\%$  for pillared clay B.  $S_{\text{CPSM}}$  values deduced through a CPSM best fit of the pertinent experimental loops is found to be practically equal to the  $S_{\text{BET(mo)}}$  values and deviates from the  $S_{\text{BET(mu)}}$  (deviation by  $11.3\%$  for A and by  $29.4\%$  for B) (refer to Table 13). Roberts' predictions of specific surface area are located far below both the  $S_{\text{BET(mo)}}$  and  $S_{\text{CPSM}}$  values (Table 13).

Parameter  $C$  for the BET (mu) equation has been determined to be  $C = 4180$ , a value unrealistically high since it predicts an extraordinary heat of adsorption. Quite to the contrary, the BET(mo) equation predicts  $C = 655$ , which is easier to accept as true as it relates to reasonable heat of adsorption values.

It is interesting to observe that due to the micropores presence, the surface area of pillared clays is comparable to that of the  $\gamma\text{-Al}_2\text{O}_3$  catalysts despite the fact that their specific pore volume is about 3 times lower than that of the alumina catalysts.

**Pore Volume and Surface Area PSD's Predictions.** Pore volume and surface area distribution predicted by the CPSM model are of a bimodal type, Figure 4(4-1d)–(4-1f) and (4-2d)–(4-2f). For pillared clay (A) a pore volume fraction of 0.53 (i.e., 0.09 out of 0.17  $\text{cm}^3/\text{g}$ ) and a surface area fraction of 0.85 (i.e., 225 out of 265  $\text{m}^2/\text{g}$ ) are found in the pore range 1.6–2.0 nm. Similarly, for pillared clay (B) a pore volume fraction of 0.33 (i.e., 0.062 out of 0.188  $\text{cm}^3/\text{g}$ ) and a surface area fraction of 0.57 (i.e., 160 out of 282  $\text{m}^2/\text{g}$ ) are located in the pore size range 1.6–2.0 nm. Due to the micropore contribution, the Roberts method, as it applies to cylindrical pore geometry with an assumed hemispherical meniscus configuration, does not yield truthful PSD predictions.

**CPSM Simulation of the Experimental Hysteresis Loops.** It is widely recognized that in pore sizes falling in the micropore region (pore widths of the order of the few molecular diameters) the Kelvin equation could not



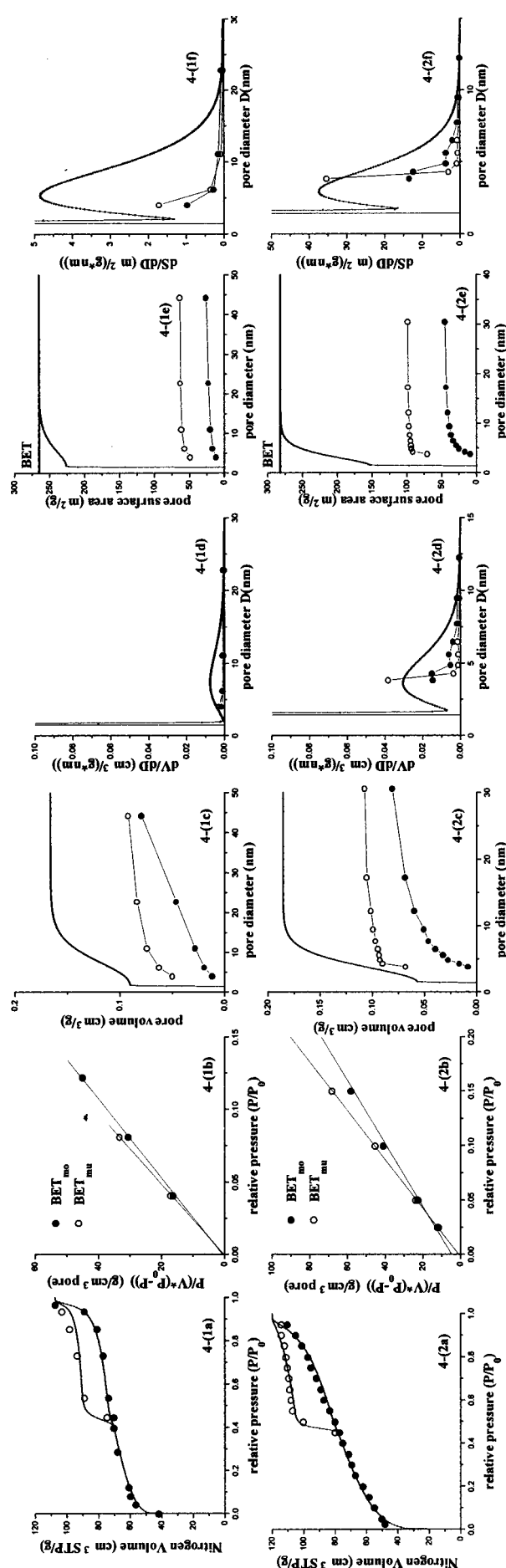


Figure 4. Nitrogen sorption hysteresis, BET data, pore volume, and specific surface area psd data for two pillared clays. Pillared clay A: (4-1a)–(4-1f). Pillared clay B: (4-2a)–(4-2f). Data point designation is identical to that noted in Figure 1.

remain valid. The values of surface tension and molar volume of the liquid adsorptive would deviate from those in the liquid bulk and even the concept of meniscus would eventually become meaningless. In cases where a mesopore–micropore system is investigated, the Kelvin equation is still applicable with regard to the mesopore portion of the pore volume. Even so, the parameters of the ordinary Kelvin equation has to assume values different from those for purely mesopore structures.

As explained in part 1 of this work (eq 11), the Kelvin equation assumes the form

$$D_K = \frac{4 V_L \gamma \cos \theta}{\ln(P_0/P)RT} \Rightarrow D_K = \frac{1.906}{\ln(P_0/P)} \cos \theta \quad (3)$$

that is valid for an l/v interface geometry varied between a hemispherical ( $\cos \theta \equiv \cos \theta_h = 1$ ) and a cylindrical one ( $\cos \theta \equiv \cos \theta_c = 0.5$ ) while the numerator is computed by  $(2 V_L \gamma / RT) = 1.906$  where  $V_L = 34.517 \text{ cm}^3/\text{gmol}$ ,  $\gamma = 8.88 \text{ mN/m}$ ,  $R = 1.987 \text{ cal/(gmol K)}$ , and  $T = 77.35 \text{ K}$  for  $[D_K] = \text{nm}$ .

Equation 3 has been successfully incorporated into the CPSM model to generate theoretical loops (part 1) and, in addition to that, to enable the fitting of experimental hysteresis loops (this part) of  $H_1$ -,  $H_2$ -, and  $H_3$ -type (IUPAC) for  $0.5 < \theta < 1.0$ . It has also become apparent, from both the theoretical and the experimental investigations of the sorption hysteresis by the CPSM model, that  $H_4$ -type loops valid for mesoporous/microporous materials can be simulated by eq 3 for  $\cos \theta < 0.5$  while the term  $(2 V_L \gamma / RT) = 1.906$  remains constant. Values of  $\cos \theta < 0.5$  bear no physical significance in interface configuration terms, the factor  $(2 V_L \gamma / RT)$  being kept constant. In such occasions encountered in  $H_4$ -type hysteresis loops, the whole product  $(2 V_L \gamma / RT) \cos \theta$  should be seen as a fitting parameter to actual experimental points. It seems that  $(\cos \theta)$  assumes extraordinarily low values while in actual fact the numerical factor 2,  $V_L$ , and  $\gamma$  might deviate from their original values. Since such envisaged deviations are not counted in terms of the numerical factor 2,  $V_L$ , and  $\gamma$ , then the overall effect is transferred to the value of  $(\cos \theta)$ .

The result of data regression by using the CPSM model is demonstrated in Figure 4(4-1a),(4-2a) and can be considered as quite satisfactory. The relevant CPSM fitting parameters are found in Table 12. The fitting of the raw hysteresis data became possible only by considering low values of  $\cos \theta_c = \cos \theta_h = 0.08$  (outside the limits 1.0–0.5). Comments on this particular observation have been included in the Discussion section of part 1 of this work. It is the presence of the micropore structure and its size interactions with the nitrogen molecule size that causes this different behavior in comparison with the relevant phenomena occurring in the mesopore structures. The CPSM simulation of the sorption phenomena is a useful tool to be used in a meaningful evaluation of the pore size distribution and the total specific surface area (Figure 4(4-1c),(4-2c),(4-1d),(4-2d)).

**MCM-41 Mesoporous Molecular Sieves.** CPSM simulation of two literature sorption hysteresis loops for MCM-41 materials<sup>5,6</sup> has been carried out. A close fit has been achieved on both sorption loops (i.e., Figure 5(5-1a),(5-2a)). The CPSM fitting parameters are tabulated in Table 14. The CPSM parameter  $N_S$  is very close

**Table 12. CPSM Fitting Parameters Referring to Hysteresis Loops of Figure 4(4-1a)–(4-2a)**

specimen	$V_{gmax}^a$ (cm <sup>3</sup> (STP)/g)	$N_S^b$	parameters of the intrinsic pore segment number distribution $F(D)$						Kelvin parameters <sup>c</sup>		adsorbed gas layer thickness parameters eq 2	
			$b_1$	$b_2$	$w_1$	$w_2$	$P_{ce}/P_0$	$(P/P_0)_{max}$	$\cos \theta_c$	$\cos \theta_h$	$m$	$n$
pillared clay A	107.4	4	−11 000	−200	1.19	1.0	0.40	0.999 475	0.12	0.12	0.00	0.36
pillared clay B	120.0	7	−11 000	−300	1.0	2.27	0.45	0.999 46	0.08	0.080	0.10	0.365

<sup>a</sup> Measurement carried out in this work (Figure 4 (4-1a)–(4-2a)). <sup>b</sup> Pore cross-sectional variation number. <sup>c</sup> As defined by eq 11 (part 1 of this work).

**Table 13. Surface Area (m<sup>2</sup>/g) Data for Pillared Clay Samples, Figure 4(4-1e)–(4-2e)**

specimen	$S_{BET(mu)}$	$C$ (BET <sub>mu</sub> parameter)	$S_{BET(mo)}$	$C$ (BET <sub>mo</sub> parameter)	$S_{Rb(co)}$	$S_{Rb(ev)}$	$S_{CPSM}$	$(S_{CPSM} - S_{BET(mo)})/S_{BET(mo)}$ (%)	$(S_{CPSM} - S_{BET(mu)})/S_{BET(mu)}$ (%)
pillared clay A	238	4181	265	655	26	89	265	0	+11.3
pillared clay B	218	218	282	281.6	50	120	282	0	+29.4

**Table 14. CPSM Fitting Parameters Referring to the Respective Hysteresis Loops of Figure 5**

specimen	$V_{\text{gmax}}$ (cm <sup>3</sup> (STP)/g)	$N_S$	parameters of the intrinsic pore segment number distribution $F(D)$								Kelvin parameters		adsorbed gas layer thickness parameters, eq 2	
			$b_1$	$b_2$	$b_3$	$w_1$	$w_2$	$w_3$	$P_{\text{ce}}/P_0$	$(P/P_0)_{\text{max}}$	$\cos \theta_{\text{c}}$	$\cos \theta_{\text{h}}$	$m$	$n$
MCM-41 (A) <sup>a</sup>	949.4	2.10	−1800	−600	−12	6.5	1.0	5.0	0.235	0.994	1.0	1.0	0.14	0.45
MCM-41 (B) <sup>b</sup>	1006.1	2.05	−2450	−600	−15	6.5	1.0	10.0	0.270	0.994	1.0	1.0	0.28	0.35

<sup>a</sup> Reference 5. <sup>b</sup> Reference 6.

to  $N_S = 2$ , indicating that individual pores possess a practically constant cross-sectional area. This fact explains the presence of a narrow hysteresis loop that does not seem to be the result of a liquid meniscus configuration change between the adsorption and desorption branch. Indeed, as  $\cos \theta_c = \cos \theta_h = 1$  an absolutely hemispherical interface prevails during both the condensation and evaporation stage.

A bimodal pore volume psd (Figure 5(5-1c)) is predicted by both the CPSM and the Roberts (i.e.,  $Rb_{(co)}$  and  $Rb_{(ev)}$ ) methods while the NLDFT predicts a unimodal psd located in the mesopore region (i.e., mean diameter  $\sim 3.6$  nm). Referring to the mesopore region, Figure 5(5-1d) provides a clear picture of the difference among the various predictions. The CPSM and the Rb method predict a mean diameter of about 2.8 nm and a second peak in the macropore range at about 80 nm.

With regard to the overall specific surface area, both BET variants predict comparable values, i.e.,  $S_{BET(mu)} = 1247$  m<sup>2</sup>/g and  $S_{BET(mo)} = 1311$  m<sup>2</sup>/g. The CPSM prediction  $S_{CPSM} = 1246$  m<sup>2</sup>/g is in an almost absolute agreement with the  $S_{BET(mu)}$  value and between those by Roberts, i.e.,  $S_{Rb(co)} = 1229$  m<sup>2</sup>/g and  $S_{Rb(ev)} = 1259$  m<sup>2</sup>/g. Quite to the contrary, the NLDFT predicts a substantially lower value, i.e.,  $S_{DFT} = 968$  m<sup>2</sup>/g as reported<sup>5</sup> (Table 2, sample Sn MCM-41). An almost complete overlapping of surface area psd's deduced by the CPSM and Rb methods is observed (Figure 5(5-1e)) while the relevant NLDFT psd is quite distinct from the rest of the psd predictions with its mean being higher by 0.8–1.0 nm.

Referring to the MCM-41 (B), Figure 5(5-2b) provides the BET plots for the multilayer and monolayer adsorption that yielded substantially different estimates of specific surface area, i.e.,  $S_{BET(mu)} = 779$  m<sup>2</sup>/g and  $S_{BET(mo)} = 1089$  m<sup>2</sup>/g. The latter value is in perfect agreement with the relevant CPSM prediction; i.e.,  $S_{CPSM} = 1089$  m<sup>2</sup>/g. Rb estimates (Table 15) are lower (i.e., by 7.5% and 4.9%) but close to the  $S_{BET(mo)}$  value. The BJH method<sup>6</sup> predicts  $S_{BJH} = 1214$  m<sup>2</sup>/g (i.e.,  $\sim 11\%$  higher than the  $S_{BET(mo)}$ ).

Bimodal pore volume psd's, Figure 5(5-2c), (5-2d), are predicted by all methods, i.e., Rb, BJH, and CPSM. One

**Table 15. Pore Surface Area (m<sup>2</sup>/g) Values Obtained from the Respective BET and Surface Area psd Data Provided from Figure 5**

	MCM-41 (A)	MCM-41 (B)
$S_{BET(mu)}$	1247	779
$C$ (BET <sub>mu</sub> parameter)	99.8	30.6
$S_{BET(mo)}$	1311	1089
$C$ (BET <sub>mo</sub> parameter)	90	16.0
$S_{BET(mo)}$	1245	1089
$C$ (BET <sub>mo</sub> parameter)	1229	1007
$S_{CPSM}$	1245	1089
$S_{Rb(co)}$	1229	1007
$S_{Rb(ev)}$	1259	1036
$S_{BJH(ev)}$		1214
$(S_{CPSM} - S_{BET})/S_{BET}$ (%)	$S_{BET(mu)}, -0.2\%$	$S_{BET(mo)}, 0\%$
$(S_{Rb(co)} - S_{BET})/S_{BET}$ (%)	$S_{BET(mu)}, -1.5\%$	$S_{BET(mo)}, -7.5\%$
$(S_{Rb(ev)} - S_{BET})/S_{BET}$ (%)	$S_{BET(mu)}, +1\%$	$S_{BET(mo)}, -4.9\%$
$(S_{BJH(ev)} - S_{BET})/S_{BET}$ (%)		$S_{BET(mo)}, +11.5\%$

peak is located at about 2.5 nm (mesopore region) and the second at about 40–60 nm, depending on the method of calculation. As Figure 5(5-2c) indicates, the cumulative pore volume  $BJH_{(ev)}$  and  $Rb_{(ev)}$  estimates coincide over the range  $D = 3$ –100 nm while the  $BJH_{(ev)}$  values are higher than those of the  $Rb_{(ev)}$  over the pore size range  $D = 3$ –30 nm. The CPSM prediction coincides with the  $Rb_{(co)}$  and  $Rb_{(ev)}$  data over the range  $D = 1$ –30 nm and goes between the two Rb branches in the range  $D = 30$ –100 nm (Figure 5(5-2c)).

**Relative Pressure versus Pore Diameter and Adsorbed Gas Layer Thickness.** In this paragraph the results of two comparisons are presented and discussed. The first concerns the functional relation between  $t(nm)$  and  $P/P_0$  as obtained in this work through the CPSM fitting of 13 experimental sorption hysteresis loops (Figure 6, dashed lines) and three literature relationships (Figure 6, solid lines). All but one CPSM predicted  $t-P/P_0$  curves lay between line (1) obtained for Halsey's correlation and line (3) as proposed by Lippens<sup>20</sup> and in general follow paths parallel to that of line (3) over the entire  $P/P_0$  range. For  $P/P_0 > 0.55$  the  $(t-P/P_0)$  curves either obtained from the literature or derived in this work follow a parallel path. For  $P/P_0 < 0.55$ , the rate of slope decrease of lines (1)<sup>7</sup> and (2)<sup>21</sup> is lower than that of the rest of the curves.

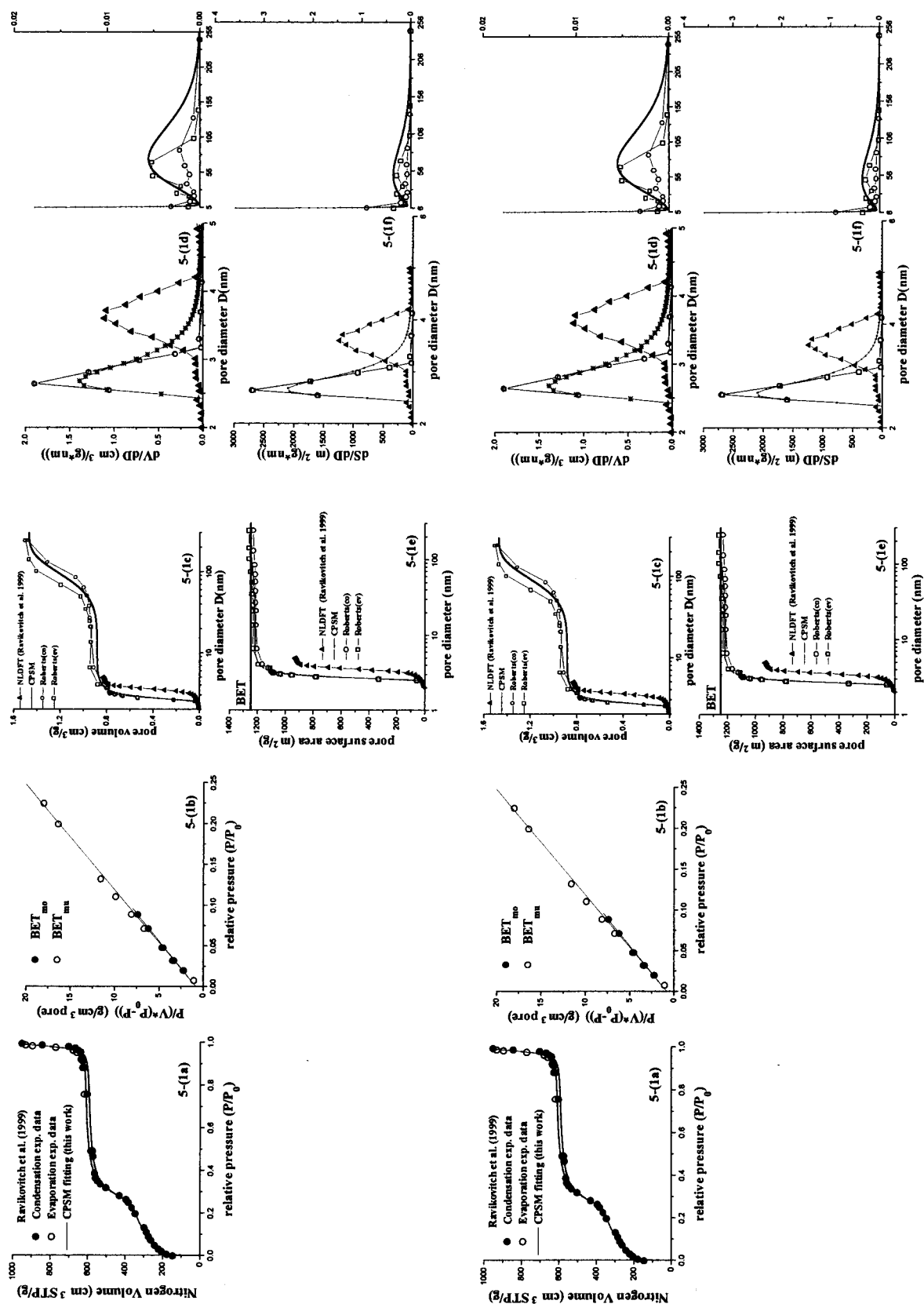


**Figure 5.** Nitrogen sorption hysteresis loop, BET (mu, multilayer; mo, monolayer), pore volume, and surface area plots for two MCM-41 mesoporous materials. MCM-41 (A), sorption data reproduced from ref 5, plots (5-1a)–(5-1f). MCM-41 sorption data ref 6, plots (5-2a)–(5-2f).

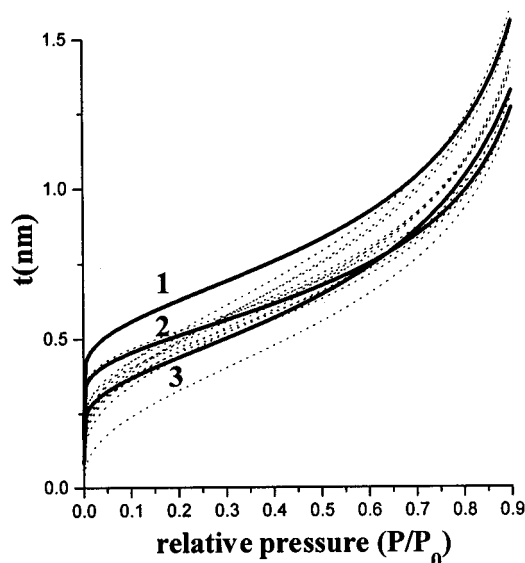


**Figure 6.** Adsorbed nitrogen multilayer thickness versus relative pressure. Solid lines: (1)  $t(\text{nm}) = 0.35(5/\ln(P_0/P))^{1/3}$ ,<sup>7</sup> (2)  $t(\text{nm}) = 0.43(5/\ln(P_0/P))^{1/3}$ ,<sup>21</sup> and (3) data of Table 1.<sup>20</sup> Dotted curves, eq 2, this work,  $t(\text{nm}) = n(5/\ln(P_0/P))^{1/3}(P/P_0)^m$ ;  $n$  and  $m$  values are provided in Tables 5, 8, 10, 12, and 14.

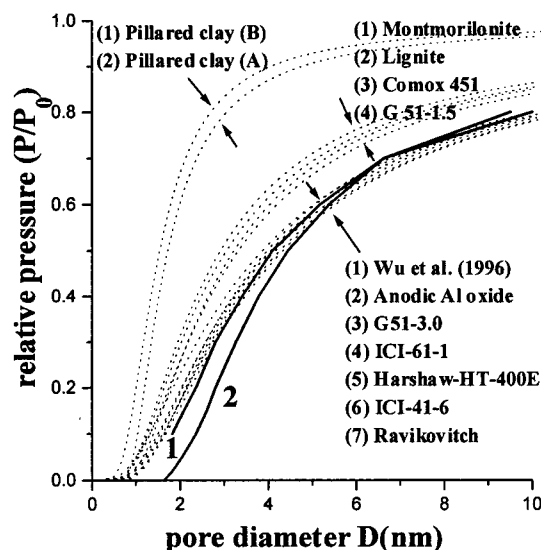


**Figure 7.** Pore size versus relative condensation pressure. Solid lines reproduced from Figure 4 of ref 23, line (1) as proposed in ref 22 and (2) as predicted by the molecular simulation model.<sup>23</sup> Dotted lines as derived in this work, by  $D(\text{nm}) = [1.906/\ln(P_0/P)] \cdot \cos \theta + 2[n(5/\ln(P_0/P))^{1/3}(P/P_0)^m]$  for the  $\cos \theta$ ,  $n$ , and  $m$  values provided in Tables 5, 8, 10, 12, and 14 for the pertinent material.

To assess the overall performance of the CPSM model by taking account of the combined effect of multilayer adsorption and capillary condensation, a second comparison has been implemented. Thus, the plots of Figure 7 have been constructed, which portray the mode of pore diameter variation with relative pressure ( $D-P/P_0$ ). Dashed lines represent CPSM predictions for the respective material noted on Figure 7, while solid lines represent literature cases. It is evident from Figure 7 that, in a major group of seven materials examined in the present investigation, the ( $D-P/P_0$ ) variation according to CPSM (i.e., Figure 7, line (1)), agree satisfactorily with the correlation proposed by Broekhoff and De Boer.<sup>22</sup> This same group of curves agree partially (i.e.,  $D > 5$  nm) with that predicted by the molecular simulation method as proposed by Sonwane and Bhatia.<sup>23</sup>

The ( $D-P/P_0$ ) curves of a second group of four materials show a clear deviation toward smaller pore sizes from the respective correlation of Broekhoff and De Boer. The latter phenomenon is the consequence of the fact that the CPSM simulation of hysteresis for the materials under consideration has been achieved for  $\cos \theta_c$  and  $\cos \theta_h \ll 1$  but still  $> 0.5$ , indicating pore geometry deviations from that of a perfectly cylindrical one. The widest deviation of the ( $D-P/P_0$ ) curve from the pertinent Broekhoff–De Boer correlation has been that for the pillared clay samples. This is again a reflection of the fact that, for this category of materials, an extremely low value of  $\cos \theta_c = \cos \theta_h = 0.08$  has been assumed to obtain a satisfactory CPSM loop fitting. The presence of microporosity and the deviation of pore geometry from that of the perfectly cylindrical one constitute a plausible reason for such a low value for the interfacial energy term of the Kelvin equation (i.e., eq 11, part 1 of this work). Therefore, the shift of the ( $D-P/P_0$ ) curves for the pillared clay materials toward smaller pore sizes (Figure 7) is explained.

It should be pointed out that the CPSM model enables the tracing of a correlation for ( $t-P/P_0$ ) and one for ( $D-P/P_0$ ) that involves the former and a Kelvin variant as a result of a hysteresis loop fitting procedure. Moreover, in the context of the latter procedure the CPSM parameter  $N_s$  can be determined. The CPSM prediction of the ( $D-P/P_0$ ) correlation is in satisfactory agreement with those based on a rigorous thermodynamic analysis.

## Discussion

The conventional methods of deducing the pore volume and surface area psd neither provide the theoretical basis for a quantitative description of the hysteresis loop nor consider the hysteresis loop as an integral whole and apply separately to one or the other branch only. The drawback of these methods is laid mainly in their deficiency to interpret appropriately the gas desorption–evaporation data and produce meaningful psd calculations. Indeed, for the materials investigated in the present study, pore surface area distributions calculated by exclusively using desorption–evaporation data predict, in the majority of the cases, pore surface areas quite far from the respective BET values. Certainly, such diverging predictions are due to the pore network structure. This phenomenon is not taken into account when the conventional methods for psd determination are applied.

Sorption hysteresis loop data include pore structure information beyond that of a pore size distribution. The complexity of pore structure, for instance, as expressed by a tortuosity factor would be the kind of information to be sought directly from gas sorption hysteresis measurements. Pore interconnections (network) do not affect directly the gas adsorption–condensation process, a fact reflected in the relative success of the conventional methods in psd evaluations when adsorption–condensation data are employed. However, the pore network structure may play an indirect role as it can control the liquid meniscus geometry and hence the respective values of the Kelvin parameter ( $\gamma \cos \theta$ ) that may not assume a single value in the course of a specified adsorption–condensation run.

The random corrugated pore, composed of several cylindrical segments connected in a series, maintains the simple pore geometry and introduces just a single parameter, i.e.,  $N_s$  the number of segments forming the



corrugated pore. In actual fact,  $N_S$  stands for the frequency of pore cross-sectional variation of an average corrugated pore, which characterizes the pore structure of a specified material.

Such a parameter may be considered as one of the main components of a pore structure tortuosity concept, although it should not be considered as the tortuosity factor in its own right. Indeed, the frequency of pore cross-sectional variation (i.e.,  $N_S$ ) should be combined with the degree of cross-sectional change in neighboring pore segments. It is obvious that the latter pore morphology property depends on the width of the pore size range over which the pore size distribution extends. It is therefore reasonable to consider that experimentally obtained values of  $N_S$  and intrinsic pore size distribution characteristics (i.e., the pore size range) can constitute the key elements for a novel definition of a pore structure tortuosity factor. Such a definition should be applicable and consistent with additional independent information, e.g., the mercury porosimetry hysteresis and particularly the mercury entrapment observations.

The simulation of the  $H_1$ -type experimental loop has been achieved by assigning  $\cos \theta_c = 0.68$  and  $\cos \theta_h = 1$ , which indicates that the CPSM theory is applied successfully without any significant deviation from the original assumptions on which the development of analytical formulas has been based. Satisfactory  $H_2$ -type hysteresis loop simulations by the CPSM model have been obtained for a pseudohemispherical  $l/v$  interface geometry prevailing during both the condensation and evaporation processes. The relatively high values of  $N_S = 4-6$  may be considered to be the causal effect. The hysteresis loops of the two naturally occurring materials, i.e., lignite and montmorillonite, belong to  $H_3$ -type and the CPSM best fitting has been implemented for a pseudocylindrical  $l/v$  interface geometry holding during the condensation–evaporation cycle. The small value of  $N_S = 2.9-3.5$  and deviations of the real pore geometry from the ideal cylindrical one may constitute a reasonable explanation of the observed phenomena.

The  $m$  and  $n$  parameters of eq 2 assume values approaching those of the original correlation, eq 1 in most of the worked examples, i.e., anodic aluminum oxide film, lignite, montmorillonite, and pillared clays. With regard to the latter parameters, the highest deviations have been determined for the six HDS catalysts. However, values of  $n$  in the range 0.35–0.43 bear a physical significance as they relate to multilayer adsorption.

It is of particular interest to note that the CPSM is a suitable analytical tool to simulate successfully sorption hysteresis loops of  $H_4$ -type obtained for mesopore–micropore structures (e.g., pillared clays) and to calculate the relevant pore volume and surface area distributions. It is also significant to mention that total specific pore surface area predicted by the CPSM is in full agreement with those of the BET method valid for monolayer adsorption. Further, it should be stressed that hysteresis loop simulation has been achieved for relatively low values of the product ( $2V_{L\gamma} \cos \theta$ ), characteristic of the prevailing interfacial tension conditions. Intrinsic pore surface areas show peaks (modes), one in the mesopore region and the second in the micropore region. The parameters of the adsorbed layer thickness are assigned values,  $m = 0-0.1$  and  $n = 0.35-0.36$ , which approach those proposed by the Halsey correlation (i.e.,  $m = 0$  and  $n = 0.35$ ).

The CPSM model has been successfully applied in simulation trials of sorption hysteresis obtained for novel mesoporous MCM-41 materials. The application of the theory yielded overall pore surface area and psd predictions that are in better agreement with the BET theory (either for multilayer or restricted adsorption) and the conventional Roberts method than with the newly reported NLDFT method. The latter, when applied to MCM-41 sorption data interpretation, predicts substantially lower surface area and a unimodal psd with a mean pore diameter equal to 3.6 nm, higher by about 0.8–1.0 nm than the pertinent CPSM prediction. Furthermore, a bimodal psd possessing one peak in the mesopore region (i.e.,  $\sim 2.8$  nm) and another in the macropore region (i.e.,  $\sim 80$  nm) have been traced by the CPSM method. It is noteworthy that the NLDFT method does not trace the macropore size peak, although such a peak exists.

From the CPSM simulations worked out in the present paper, it turns out that the overall range of variation of the adsorbed layer thickness parameters is  $m = 0-0.28$  and  $n = 0.35-0.45$ . The relevant ( $t$  vs  $P/P_0$ ) curves follow a pattern parallel to that reported by Lippens et al.<sup>20</sup> For the majority of materials studied (exempting those possessing microporosity), CPSM-predicted pore diameter versus  $P/P_0$  curves are in good agreement with the relevant data reported by Broekhoff and De Boer<sup>22</sup> and in partial agreement with those predicted by the molecular simulation method.<sup>22</sup>

The CPSM nitrogen model, as attested to in this work, is simple in form, flexible to apply, and purely analytical to simulate experimental capillary hysteresis data, deduce information concerning pore structure tortuosity characteristics, and predict a pore size versus relative pressure correlation in good agreement with relevant literature data.

## Conclusion

The corrugated pore structure model (CPSM) has been successfully applied in the simulation of experimental nitrogen sorption hysteresis loops for a good variety of porous materials covering the full range of loop types under IUPAC.

In general, CPSM predictions of intrinsic pore volume and surface area distributions prove to be superior compared to those obtained by the Roberts method. However, in certain cases the latter method when applied to the adsorption–condensation data predicted psd's in satisfactory agreement with the respective CPSM ones.

CPSM-predicted total specific surface areas are in perfect agreement with BET values. Nevertheless, in certain cases involving microporosity, the agreement was closer to values obtained with the restricted adsorption BET variant (monolayer adsorption) rather than with the BET multilayer model.

With regard to MCM-41 materials, the CPSM model predicts intrinsic psd's and total surface areas in better agreement with those by the BJH method than with the NLDFT method. The latter method predicted an appreciably lower total surface area and higher (by about 1 nm) mean pore diameter as explained in the Discussion section.

The fitting of the experimental loops has been achieved for  $t$  vs  $P/P_0$  correlations that compare well with those reported in the literature.

CPSM simulation of experimental sorption data indicated that the majority of  $N_S$  values falls in the range  $N_S = 2-7$ . One should be reminded that the theoretical simulations (part 1) showed that  $N_S$  varied in the range 2–10, an exception being the value  $N_S = 30$  for H<sub>2</sub>-type hysteresis (IUPAC). For each specific material a satisfactory fitting was achieved for a single value of  $N_S$ .

The CPSM model is a general, flexible, and purely analytical tool that, through a satisfactory fitting of the entire sorption hysteresis loop, can generate information suitable for an assessment of pore structure tortuosity.

## Acknowledgment

The authors are grateful to the State Scholarships Foundation of Greece for the financial assistance offered to one of them (C.S.).

## Nomenclature

$A$  = ampere  
 $b$  = parameter of the intrinsic pore segment number distribution function  $F(D)$  (eq 31, part 1 of this work)  
 $b_i = b$  parameter of a unimodal BSD distribution to be used in the synthesis of a multimodal psd  
 $C$  = BET equation parameter  
 $C_b$  = coulomb  
 $d_p$  = particle size  
 $m$  = exponent in eq 2  
 $N_S$  = number of segments comprising a corrugated pore (frequency of pore cross-sectional area variation)  
 $n$  = multiplication factor in eq 2  
 $P/P_0$  = relative pressure of adsorption gas  
 $P_{CE}/P_0$  = critical relative pressure indicative of capillary evaporation termination  
 $S_{BET}$  = specific surface area calculated by the BET theory ( $m^2/g$  or  $m^2/m^2$  foil)  
 $S_{CPSM}$  = specific surface area calculated through the simulation of nitrogen sorption hysteresis data by the CPSM model  
 $S_g$  = specific surface area of a commercial catalyst sample.  
 $S_{Rb(co)}, S_{Rb(ev)}$  = specific surface area computed by the Roberts method applied to the capillary condensation or evaporation branch of the hysteresis loop, respectively  
 $t$  = thickness of adsorbed gas layer.  
 $V$  = volt  
 $V_{gmax} \rightarrow 1$  = maximum volume of gas (STP) adsorbed at  $P/P_0 \rightarrow 1$   
 $V_p$  = pore volume ( $m^3/g$ ) or ( $m^3/m^2$  foil)  
 $W$  = relative weight of a unimodal BSD used in the synthesis of multimodal psd's

## Acronyms

BSD = bell-shaped distribution  
 CPSM = corrugated pore structure model  
 IUPAC = International Union for Pure and Applied Chemistry  
 NLDFIT = non-local-density functional theory<sup>5</sup>

## Literature Cited

(1) Barrett, L. P.; Joyner, L. G.; Halenda, P. P. The Determination of Pore Volume and Area Distributions in Porous Substances. 1. Computations from Nitrogen Isotherms. *J. Am. Chem. Soc.* **1951**, *73*, 373–380.

- (2) Brunauer, S.; Mikhail, R. Sh.; Bodor, E. E. Pore Structure Analysis without a Pore Shape Model. *J. Colloid Interface Sci.* **1967**, *24*, 451–463.
- (3) Cranston, R. W.; Inkley, F. A. The Determination of Pore Structures from Nitrogen Adsorption Isotherms. *Advances in Catalysis*; Academic Press: New York, 1977; Vol. 9, pp 143–153.
- (4) Roberts, B. F. A Procedure for Estimating Pore Volume and Area Distributions from Sorption Isotherms. *J. Colloid Interface Sci.* **1967**, *23*, 266–273.
- (5) Ravikovitch, P. I.; Haller, G. L.; Neimark, A. V. Density Functional Theory for Calculating Pore Size Distributions: Pore Structure of Nanoporous Catalysts. *Adv. Colloid Interface Sci.* **1998**, *76–77*, 203–226.
- (6) Wu, C. N.; Tsai, T. S.; Liao, C. N.; Chao, K. J. Controlling Pore Size Distributions of MCM-41 by Direct Synthesis. *Microporous Mater.* **1996**, *7*, 173–185.
- (7) Halsey, G. D. *J. Chem. Phys.* **1948**, *16*, 931.
- (8) Gregg, S. J.; Sing, K. S. W. *Adsorption Surface Area and Porosity*, 2nd ed.; Academic Press: London, 1982.
- (9) Itaya, K.; Sugawara, S.; Arai, K.; Saito, S. Properties of Porous Aluminum Oxide Films as Membranes. *J. Chem. Eng. Jpn.* **1984**, *17*, 514–520.
- (10) Randon, J.; Mardilovich, P. P.; Govyadinov, A. N.; Paterson, R. Computer Simulation of Inorganic Membrane Morphology. Part 3. Anodic Alumina Films and Membranes. *J. Colloid Interface Sci.* **1995**, *169*, 335–341.
- (11) Chen, J. J.; Ruckenstein, E. Sintering of Palladium on Alumina Model Catalyst in a Hydrogen Atmosphere. *J. Catal.* **1981**, *69*, 254–273.
- (12) Paternaraki, G.; Pavlidou, C. Catalysis over Porous Anodic Alumina Catalysts. *J. Catal.* **1994**, *147*, 140–155.
- (13) Salmas, C. E. Hydrodesulfurization of Oil Fractions on a Catalyst with a Regular Pore Structure. Doctoral Thesis. Department of Chemical Engineering, National Technical University of Athens (NTUA), Athens, Greece, in preparation.
- (14) Skoulikidis, Th.; Batzias, F. Structure Secondaire Des Alumines Actives Préparées Electrolytiquement. In *4<sup>th</sup> International Congress for the Study of Bauxites, Alumina and Aluminum*, Athens, Greece; 1978; Vol. 3, p 1037.
- (15) Cosgrove, L. A. Porosity of Anodic Oxide Coatings on Aluminum. Comparison of *n*-Butane and Krypton Sorption. *J. Phys. Chem.* **1956**, *60* (4), 385–388.
- (16) Zwietering, P.; Van Krevelen, D. W. *Fuel* **1954**, *33*, 331–337.
- (17) Lin, J. S.; Hendricks, R. W.; Harris, L. A.; Yust, C. S. *Appl. Crystallogr.* **1978**, *11*, 621.
- (18) Kaloidas, V.; Koufopoulos, C. A.; Gangas, N. H.; Papayannakos, N. G. Scale-up Studies for the Preparation of Pillared Layered Clays at 1kg per Batch Level. *Microporous Mater.* **1995**, *5*, 97–106.
- (19) Stathopoulos, V. N.; Ladavos, A. K.; Kolonia, K. M.; Scaribas, S. P.; Petrakis, D. E.; Pomonis, P. J. Preparation, Characterization and Surface Acid Catalytic Activity of Microporous Clays Pillared with  $Al_{1-x}Fe_xO_y$  ( $x = 0.00$  to  $1.00$ ) Oxidic Species. *Microporous Mesoporous Mater.*, **1999**, *1–2*, 111–121.
- (20) Lippens, B. C.; Linsen, B. G.; De Boer, J. H. Studies of Pore Systems in Catalysis I. Adsorption of Nitrogen; Apparatus and Calculations. *J. Catal.* **1964**, *3*, 32–37.
- (21) Wheeler, A. *Catalysis*; Reinholds: New York, 1955; Vol. 2, p 116.
- (22) Broekhoff, J. C. P.; De Boer, J. H. Studies on Pore Systems in Catalysts IX. Calculation of Pore Distributions from the Adsorption Branch of Nitrogen Sorption Isotherms in the Case of Open Cylindrical Pores A. Fundamental Equations. *J. Catal.* **1967**, *9*, 8–14.
- (23) Sonwane, C. G.; Bhatia, S. K. Adsorption in Mesopores. A Molecular Continuum Model with Applications to MCM-41. *Chem. Eng. Sci.* **1998**, *53*, 3143–3156.

Received for review February 2, 2000

Revised manuscript received June 13, 2000

Accepted June 20, 2000

IE000163W